Engineering Notebook: Rocket Engine

Asa Gangjee - Application Reference Number 688239119

2024-2025

Abstract

This engineering notebook presents the design, simulation, and testing of a regeneratively cooled aerospike rocket engine fabricated entirely through resin-based 3D printing. The objective was to demonstrate that high-fidelity hot-fire testing can be achieved with a fully polymer prototype produced for under one hundred dollars. Using NASA CEA data and ANSYS Fluent, the aerospike contour was refined through iterative CFD modeling until the simulated thrust matched analytical predictions within one percent. The final engine, cooled with liquid propane, achieved a measured thrust of 113.27 N and a 55 percent reduction in wall temperature compared to an uncooled design at the cost of $87.99 per engine. The work validates polymer additive manufacturing as a practical, low-cost pathway for iterative propulsion development and proves that accurate thermal and performance testing can be conducted using accessible materials and infrastructure.

Document Overview

All simulations, data, and figures in this notebook correspond directly to the engine tested between August 2024 and March 2025. The accompanying Maker Portfolio video provides a visual summary of CFD results, fabrication workflow, and live test-fire data.

1 Background

Since the earliest liquid-fueled rocket engines of the 20th century, cost and manufacturability have remained major barriers to propulsion system innovation. The first generation of regeneratively cooled engines, including the V-2 developed by the German Army in the 1940s, used complex copper cooling channels brazed into heavy steel walls [1]. While this design enabled sustained combustion, it required extensive machining and skilled labor. Even small test articles cost thousands of dollars to produce, making iterative design prohibitively expensive. This limited progress in experimental rocket development to large government-funded programs for much of the 20th century.

By the 1960s, NASA and other research institutions sought to improve engine performance across varying altitudes, leading to the invention of the aerospike nozzle [2]. Unlike conventional bell nozzles, which are optimized for a single design altitude, the aerospike uses the surrounding atmosphere to shape its exhaust expansion, maintaining near-optimal efficiency from sea level to vacuum. Monokrousos et al. demonstrate that 50% of the efficiency loss of conventional nozzles [3] can be recouped with an aerospike-type engine geometry. However, the geometry of the aerospike introduces new challenges. The central spike must withstand extreme thermal and mechanical loads, and until recently, no cost-effective way existed to incorporate regenerative cooling channels within the spike or nozzle wall [4]. Traditional methods like CNC machining or brazing could not fabricate the intricate internal geometries required.

Regenerative cooling is a thermal management method in which the engine propellant is circulated through channels embedded within the chamber and nozzle walls before combustion. As the coolant flows through these channels, it absorbs heat from the engine structure, lowering wall temperatures while preheating the propellant prior to injection. This improves thermal efficiency, structural longevity, and combustion stability, allowing sustained operation under high heat flux.

The main advantage of regenerative cooling is its ability to maintain wall temperatures below material limits without the need for external coolants. By transferring heat into the propellant, the system recovers energy that would otherwise be lost and reduces the total cooling mass required. The method also enables thinner wall construction, reducing overall engine weight and improving response to transient heating.

In most liquid-fueled rocket engines, the fuel is circulated through helical or longitudinal channels that trace the highest heat flux regions near the throat and along the expansion contour. The absorbed heat raises the propellant's enthalpy while preventing structural failure from localized thermal loading. Early engines such as the German V-2 used regenerative circuits constructed from brazed copper channels, and later designs like the F-1 and RS-25 refined this technique for continuous operation under heat fluxes exceeding 10 $\mathrm{MW/m^2}$ [2, 5].

Beginning in the 2010s and accelerating in the early 2020s, aerospace startups and additive manufacturing vendors began to revive the aerospike concept by exploiting the geometric freedom of metal powder bed fusion and related metal additive manufacturing (AM) approaches. Metal additive manufacturing removed a primary historical barrier: the inability to form highly intricate internal cooling channels and thin, contoured walls in a single piece. Several contemporary efforts demonstrate that selective laser sintering and laser powder bed fusion of copper and copper alloys can produce aerospike geometries with integrated cooling passages that would have been prohibitively expensive or infeasible with traditional subtractive methods [6, 7].

Two notable industry efforts exemplify this modern trend. Pangea Aerospace utilized metal 3D printing to build and hot-fire test a methalox aerospike demonstrator, publishing test milestones and engine imagery that document an iterative metallurgical and AM post-processing workflow [7, 8]. Independently, LEAP 71 announced a rapid design, AM production, and hot-fire test cadence for small aerospike engines, utilizing a proprietary AI-driven design loop and laser powder bed fusion fabrication on a compressed schedule in late 2024 and early 2025 [9, 10]. It should be noted that the present project was the first to demonstrate, to the best of the authors' knowledge, a pressure-fed, regeneratively cooled aerospike hot-fire test, performed on December 7, 2024.

While the work of LEAP 71 and Pangea demonstrates the maturity of metal additive manufacturing for aerospike applications, there remains limited investigation into the use of thermopolymers as transient test articles for propulsion research. Although the heat deflection and glass transition temperatures of most thermopolymers are far below theoretical steady-state wall temperatures of 700–900 K reported by Song et al. [11], their controlled softening behavior under thermal load allows for valuable insight into early-stage engine behavior. High-temperature thermopolymers are available in both transparent and opaque formulations, making them uniquely suited for optical diagnostics. Through the use of clear polymer structures, intra-chamber combustion dynamics, flow separation along the spike contour, and coolant flow distribution within regenerative channels can be visualized directly. Such visual access is unattainable in metallic engines, where measurements rely solely on indirect sensing.

The capability to observe and record these phenomena using high-speed and infrared imaging provides an experimental pathway for validating computational fluid dynamics and conjugate heat-transfer models in regimes where traditional instrumentation is impractical. Additionally, fluid flow throughout the regenerative cooling channels can be easily visualized with thermopolymer prototypes. Thermopolymer prototypes thus bridge the gap between simulation and full-scale metal testing, enabling researchers to empirically capture transient heating, plume expansion, and film-cooling behavior in real time.

Resin-based 3D printing processes such as stereolithography (SLA) and fused filament fabrication (FFF) enable these optical and thermal studies to be carried out at a fraction of

the cost and lead time of selective laser sintering or metal AM. The affordability of desktop-scale SLA systems eliminates reliance on third-party manufacturers and allows rapid iteration of regenerative geometries, injector configurations, and chamber dimensions directly from digital models.

This research aims to evaluate the feasibility of SLA-printed thermopolymer engines for transient hot-fire testing of regeneratively cooled aerospike configurations. The use of Formlabs High Temp V2 resin, with a heat deflection temperature of 238°C [12], allows the production of semi-transparent components capable of short-duration operation under realistic combustion conditions. By correlating observed surface deformation, discoloration, and flow visualization data with numerical predictions, this work seeks to establish whether low-cost polymer fabrication can withstand short transient testing, and be used to create functional regeneratively cooled rocket engines. If successful, the method would extend experimental access to thermal and fluid phenomena within rocket chambers, improving both the speed and fidelity of early-stage propulsion development while reducing dependence on costly metal prototypes and gas imaging.

1.1 Thesis

This project investigates the use of resin-based 3D printing as a low-cost manufacturing pathway for high-performance bipropellant rocket engines. This project will produce a regeneratively cooled SLA-printed aerospike rocket engine, and test that prototype under transient conditions. The goal is to demonstrate that accurate, repeatable hot-fire testing can be achieved using a fully polymer engine fabricated for under $100 unit and producable in less than two days.

2 Criteria & Constraints

Constraint	Reasoning
Time	Due to the complexity of this project, time is the most stringent constraint. I should be conservative when accounting for third-party manufacturing or shipping delays.
Cost	This project operates on a limited budget of $\$1,550$, constraining component selection and fabrication options.
Parts	Only consumer-available parts may be purchased, restricting the design of the gas delivery system and overall engine configuration.
Materials	Material choices must balance temperature tolerance, machinability, and availability within my resources.
Part Size	The design is limited to parts which fit in a $145 \times 145 \times 185$ mm print volume, as that is the maximum allowed by the SLA printer available to me [13].

Criterion	Reasoning
Produce 90% **of peak thrust**	Defines the minimum performance benchmark for engine validation.
Speed of manufacturing	The final engine design must be manufacturable in less than 48 hours to prove SLA printing provides a faster alternative to traditional manufacturing methods.
Thrust stand accuracy	Accurate measurement is required for valid analysis of thrust performance.
Thrust stand precision	Precision ensures consistency and repeatability across test runs.
Robust prototype	The engine must endure multiple hotfires without structural or performance degradation.
Aerospike internal geometry	The final design must incorporate an aerospike nozzle to validate the intended flow and cooling behavior.

3 Design Decision Literature Review

To fully define the problem and understand the fundamental science behind aerospike rocket engine design, fabrication, simulation, and testing, I conducted significant background research before beginning the project. This was especially necessary as I did not have a faculty overseer specialized in propulsion systems, and design failures can be catastrophic. A thorough understanding of how to mitigate risks in both design and testing was therefore essential.

3.1 Nozzle Truncation

Computational study on flow through truncated conical plug nozzle with base bleed experimentally demonstrates the advantages of a "truncated" nozzle design, where the spike of the aerospike is cut off to create a blunt end [14]. The paper concluded that a 40% truncated nozzle with a base bleed effectively mimics the performance characteristics of a full-length canonical aerospike nozzle. It also showed that a correctly truncated nozzle can minimize flow separation between the converging exhaust streams if a "bubble" of low-pressure air is trapped between the truncated portion of the nozzle and the exhaust flow.
The findings of this paper were highly influential for me, as I chose to truncate the nozzle in preliminary sketches as truncation allowed a larger design to fit within the build constraints of the resin 3D printer. However, the flow separation observed in CFD with potential truncated designs (see Figure 1) resulted in too great of a performance loss, so a full-length spike design was pursued.

3.2 Material Choice

I selected high-heat resin for the early hot-fire prototypes of the rocket engine, specifically High Temp V2 Resin From Formlabs [15]. This material was chosen because of its high thermal conductivity for a thermopolymer resin, which is ideal for an effective regenerative cooling system, its lack of post-print processing, and its commercial availability. The main limitation of the resin is its low tensile strength of 51.1 MPa, which prevents a design with a standard chamber pressure for amateur rocket engines [15].

3.3 Design Process and Calculations

To understand the calculations behind sizing and designing an aerospike rocket engine, I studied *How to Design, Build, and Test Small Liquid-Fuel Rocket Engines* by Leroy Krzycki [16]. This guide provided detailed explanations of engine fabrication, test-stand construction, and operational safety. It gave me a realistic sense of project scope and clear milestones to ensure completion within the desired timeframe.

I also used the text, along with industrial safety publications, to plan the high-pressure gas system of the test bed. Precautions such as installing ball

valves, flashback arrestors, and using only brass high-pressure piping were implemented to minimize risks of oxygen leaks, ignition, or backflow. Krzycki's methodology also informed my selection of internal and external engine geometries. To familiarize myself with the process, I performed a mock sizing exercise for a rocket engine designed to fit the constraints of the University of Alabama at Huntsville's rocket test bed [17].

4 Simulation

As is industry standard, preliminary simulations were used to guide the design process before manufacturing. ANSYS was chosen for the CFD software as the free student version has robust capabilities. Simulations beginning with Section 4.5 were conducted with a multi-core, enterprise-level licensed ANSYS suite which I individually solicited from the company.

4.1 Simulation Background Research

I decided to use a 2-D CFD simulation of the engine exhaust flow to analyze the performance of each potential design derived from the rocket design equations. I first used NASA CEA (Chemical Equilibrium Analysis) to predict key engine performance parameters, then used a spreadsheet implementing the equations from *How to design, build and test small liquid-fuel rocket engines* (1967) to get 2-D sketch parameters [16]. These equations were modified to accommodate an aerospike geometry, with an annular area calculation replacing the standard circular formulation.

I chose to design iteratively, starting from the parameterized values, then evaluating exhaust performance in CFD and adjusting the contour to improve exhaust adhesion to the spike surface. This iterative method was selected over a reverse Prandtl–Meyer approach because the manufacturing tolerances of the available printers and the design mass flow rates resulted in very small annular areas [18]. This geometry produced a nonconstant radius shroud contour, which significantly complicates a reverse Prandtl–Meyer-based design process.

To better understand the sizing and simulation process for an aerospike rocket engine, I conducted practice solutions using a simplified plug engine design [19]. This simplified case allowed me to compare the CFD simulation with a geometry that has a known analytical contour. I used resources from the YouTube channel *VDEngineering* [20], along with the paper *Computational study on flow through truncated conical plug nozzle with base bleed* [14], to inform the CFD workflow for the practice solution. All practice simulations followed the CFD workflow described in Section 4.2.

4.2 Simulation Design Workflow

1. **Define Engine Parameters:** Select a target thrust, chamber pressure P_0, and combustion temperature T_0 for the engine.
2. **CEA Analysis:** Run NASA CEA (Chemical Equilibrium Analysis) to obtain the expansion ratio, specific impulse, and exhaust properties (see Appendices A, B, and C). Use the pressure ratio $\left(\frac{P_0}{P_{\text{air}}}\right)$ to estimate the expansion ratio.
3. **Analytical Calculations:** Plug the computed values into the design spreadsheet implementing the governing rocket design equations as defined by Krzycki [16]. Verify consistency with expected mass flow rate, thrust, and exit Mach number.
4. **Preliminary Troubleshooting:** Check for unreasonable outputs or parameter conflicts before geometry creation.
5. **Geometry Creation:**
   (a) In ANSYS DesignModeler, create a 2-D sketch of the nozzle contour and constrain the sketch to confirm valid dimensions. Make sure that the outlet is greater than 5 spike diameter lengths away from the engine cowling to mitigate reverse flow interactions.
   (b) Convert the sketch into a surface.
   (c) Split the surface into logical zones.
6. **Meshing:**
   (a) Open the geometry in the Meshing application.
   (b) Apply face meshing to each split zone.
   (c) Use side sizing to achieve fine mesh density, aiming for approximately 1×10^5–3×10^5 vertices depending on the test tunnel domain.
   (d) Concentrate mesh refinement in the compression region and in the zone between the end of the cowling and the spike tip, where shock structures are most sensitive.
   (e) Name boundaries: `inlet`, `outlet`, `farwalls`, and `rocketwalls` with the named selection tool.
7. **Solver Setup:**
   (a) In the setup window, enable double precision and multicore processing (2 core student version max).
   (b) Choose a density-based solver.
   (c) Enable the energy equation.
   (d) Select the realizable k–ε turbulence model.

(e) Set fluid density to ideal gas and viscosity to Sutherland law.

8. **Boundary Conditions:**

   (a) Define `inlet` as a pressure inlet with gauge total pressure equal to the chamber pressure from Step 1, and initial gauge pressure such that V_0 is the injector velocity of the design.

   (b) Set `outlet` as a pressure outlet at ambient (sea-level) pressure.

   (c) Apply wall conditions to `rocketwalls` and `farwalls`.

   (d) Set inlet total temperature to the T_0 from CEA, and outlet static temperature to ambient.

   (e) Set the operating pressure to 0 Pa and ensure gravity is disabled.

9. **Numerical Controls:**

   (a) Tighten convergence criteria so that all residuals drop below 1×10^{-4}.

   (b) Adjust the ratio of specific heats γ and Courant number if solutions converge unrealistically fast or diverges.

   (c) Use the Roe-FDS flux scheme with a least-squares cell-based gradient.

   (d) Set all spatial discretization methods to second-order upwind.

10. **Initialization and Run:**

    (a) Perform standard initialization from the pressure inlet.

    (b) Verify reasonable initial values for velocity and pressure.

    (c) Run a mesh check; correct any quality warnings before solving.

    (d) Continue iterations until convergence is achieved (typically 4,000–8,000 iterations).

    (e) Record the y^+ of the mesh to verify simulation accuracy.

11. **Post-Processing:**

    (a) Visualize pressure, temperature, and Mach contours to inspect flow structures.

    (b) Compare simulation results with design parameters.

    (c) Save data and record mesh statistics.

12. **Troubleshooting Guidelines:**

    - If flow detaches near the spike lip (faster exit, poor adherence), the design is overexpanded.
    - If flow fails to reach the spike or separates early (sluggish exit flow), the design is underexpanded.
    - If the simulation runs excessively slowly, the mesh is likely too fine or requires more aggressive structuring.

4.3 Practice Solution 1:

Parameter	Value
Total mass flow, $\dot{m}$	1.398 $\mathrm{kg\,s^{-1}}$
Oxidizer mass flow, $\dot{m}_{\mathrm{O_2}}$ (O/F=2.20)	0.971 $\mathrm{kg\,s^{-1}}$
Fuel mass flow, $\dot{m}_{\mathrm{CH_4}}$ (O/F=2.20)	0.427 $\mathrm{kg\,s^{-1}}$
Mixture ratio, O/F	2.20
Ratio of specific heats, γ (chamber)	1.1826
Chamber temperature, T_c	3358 K
Chamber pressure, P_0	14, 340, 000 Pa
Throat area, A_t	484.613 $\mathrm{mm^2}$
Ambient pressure, P_a	101 000 Pa
Thrust, F_T (idealised, $\dot{m} \cdot v_e$)	2974.6 N
Chamber volume, V_{chamber}	69, 687.3 $\mathrm{mm^3}$
Specific impulse, $I_{sp,\mathrm{vac}}$	338.63 s

Table 1: CEA and analytical design parameters for plug engine.

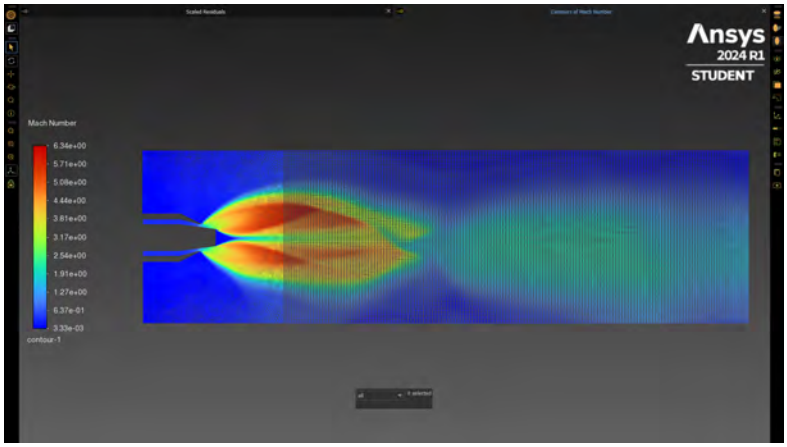

Figure 1: Mach contours of practice solution 1.

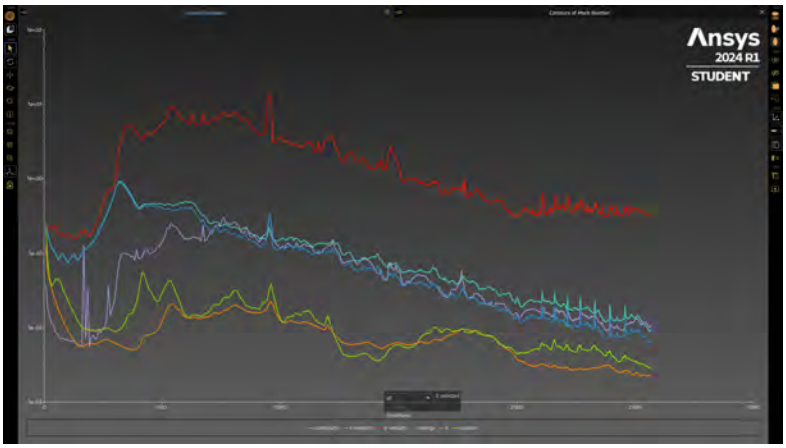

Figure 2: Residuals plot of practice solution 1, for full CEA output, reference Appendix A.

Figures 1 and 2 depict the Mach contours and residuals plot of the example solution. While the initial simulations served as a starting point for further analysis, the outputs were poor. The mesh quality was low due to an under-zoned model, which reduced the overall accuracy of the simulation. Additionally, the example solution incorporated a cowl that significantly under-expanded the exhaust flow. As a result, the exhaust failed to reattach after the low-pressure zone created by the truncation. These issues were identified and corrected in subsequent simulations.

4.4 Practice Solution 2

For the second practice solution, I created a more structured mesh by sub-dividing the zones more aggressively using the Face Split tool in DesignModeler. With this finer discretization, a higher quality mesh was obtained, as shown in Figure 3. More realistic values for the engine parameters (see Appendix B) relevant to this project were also used for the simulation, as listed in Table 2. Finally, the exhaust contours were labeled to identify key regions of aerospike exhaust flow and to verify the accuracy of the simulations, as shown in Figure 4 and Figure 5.

Parameter	**Value**
Total mass flow, $\dot{m}$	0.013557 $\mathrm{kg\,s^{-1}}$
Oxidizer mass flow, $\dot{m}_{\mathrm{O_2}}$ (O/F=2.20)	0.009320 $\mathrm{kg\,s^{-1}}$
Fuel mass flow, $\dot{m}_{\mathrm{CH_4}}$ (O/F=2.20)	0.004237 $\mathrm{kg\,s^{-1}}$
Mixture ratio, O/F	2.20
Ratio of specific heats, γ (chamber)	1.1435
Chamber temperature, T_c	3041.25 K
Chamber pressure, P_0	289 580 Pa
Throat area, A_t	292.90 $\mathrm{mm^2}$
Ambient pressure, P_a	101 000 Pa
Thrust, F_T (idealised, $\dot{m} \cdot v_e$)	23.59 N
Chamber volume, V_{chamber}	23 794.0 $\mathrm{mm^3}$
Specific impulse, $I_{sp,\mathrm{vac}}$	177.5 s

Table 2: CEA and analytical design parameters for plug engine.

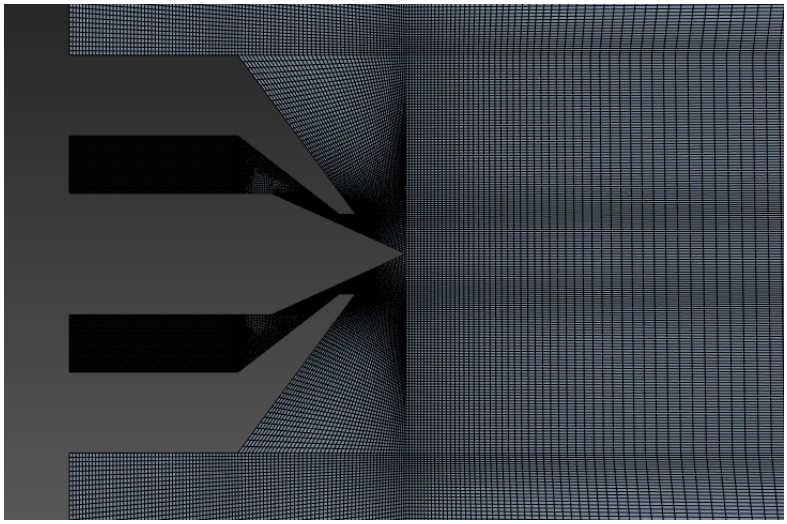

Figure 3: Mesh of practice solution 2.

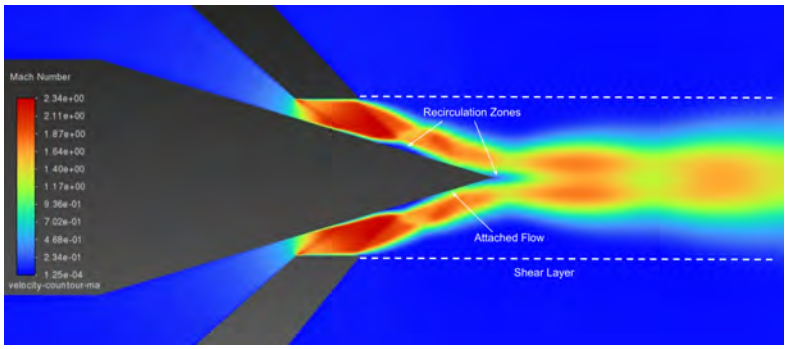

Figure 4: Mach contours of practice solution 2.

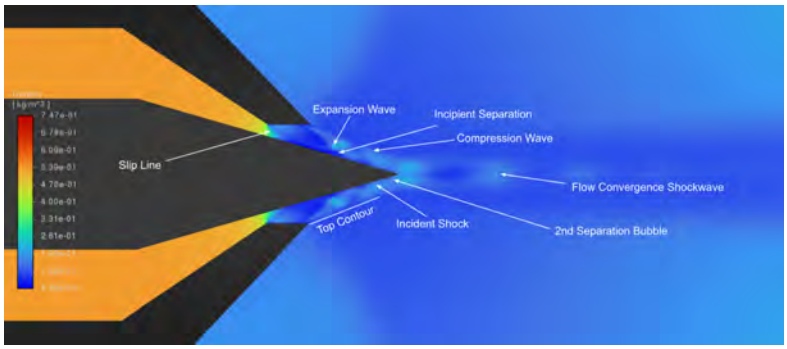

Figure 5: Density contours of practice solution 2.

While these simulations were of much higher quality, I observed some exhaust contour "drooping," which I attributed to using a planar simulation instead of an axisymmetric simulation. For the final design, I used an axisymmetric setup with the axis of symmetry aligned along the contour line of the aerospike engine. This approach is valid because an annular aerospike is symmetric about its central axis and can, therefore, be accurately simulated using an axis of symmetry that bisects its 2-D sketch. This approach is consistent with the simulation completed by Nair et al. in *Computational study on flow through truncated conical plug nozzle with base bleed* [14].

4.5 Final Design:

Parameter	**Value**
Total mass flow, $\dot{m}$	$0.04700\ \mathrm{kg\,s^{-1}}$
Oxidizer mass flow, $\dot{m}_{\mathrm{O_2}}$ (O/F = 2.00)	$0.03133\ \mathrm{kg\,s^{-1}}$
Fuel mass flow, $\dot{m}_{\mathrm{CH_4}}$ (O/F = 2.00)	$0.01567\ \mathrm{kg\,s^{-1}}$
Mixture ratio, O/F	2.00
Ratio of specific heats, γ (chamber)	1.1634
Chamber temperature, T_c	3027.58 K
Chamber pressure, P_0	723 950 Pa
Throat area, A_t	$118.08\ \mathrm{mm^2}$
Exit area, A_e	$216.04\ \mathrm{mm^2}$
Area ratio, A_e/A_t	1.8296
Ambient pressure, P_a	101 000 Pa
Exit velocity, v_e (CEA printed, used here)	$2156.2\ \mathrm{m\,s^{-1}}$
Thrust, F_T	118 N
Specific impulse (exit), $I_{sp} = v_e/g_0$	219.87 s
Exit Mach number (CEA)	1.953
Chamber volume, V_{chamber}	$98\,059.58\ \mathrm{mm^3}$

Table 3: CEA and analytical design parameters for aerospike engine.

For the final design, I used the CEA outputs shown in Appendix C to inform a contour sketch in DesignModeler, as shown in Figure 6. The sketch was then meshed with a high-density structured mesh, shown in Figure 7. I simulated the exhaust flow at both sea level and at an altitude of 25 km to verify that the exhaust flow reattached over a wide range of ambient pressure ratios. This aerospike was designed for a chamber pressure of 723 kPa and an oxidizer-to-fuel ratio of 2:1, using gaseous oxygen and liquid propane as propellants.

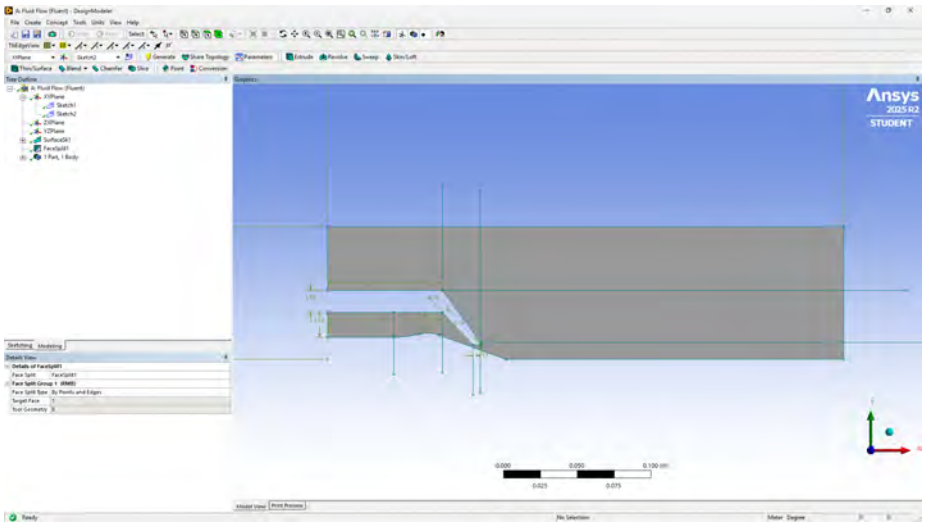

Figure 6: 2-D sketch of final design.

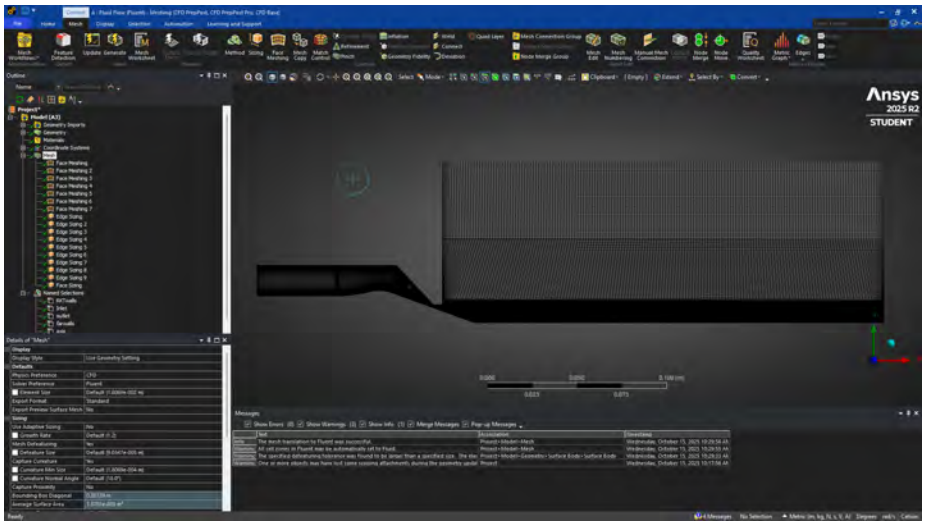

Figure 7: Structured mesh of final design.

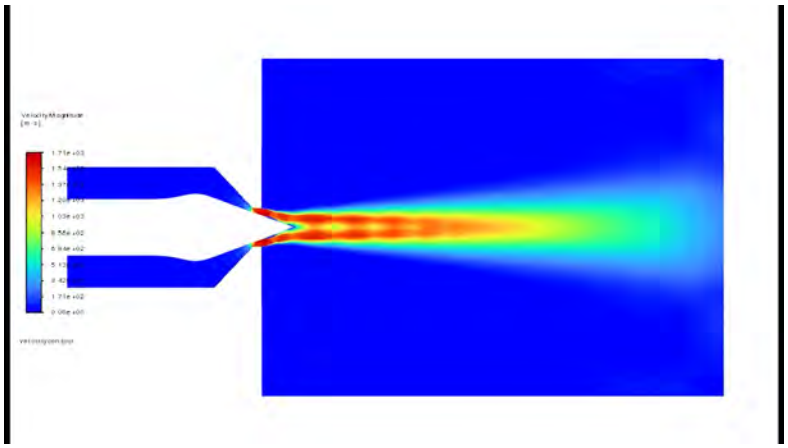

Figure 8: Velocity contours of final design at sea level($P_0 = 101,325$ Pa).

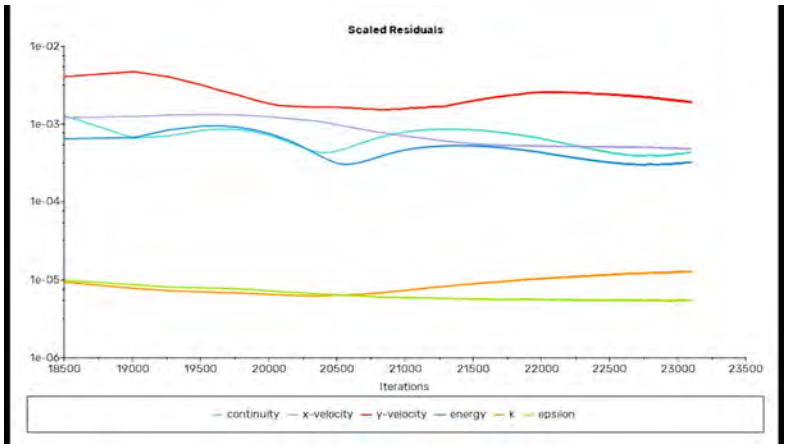

Figure 9: Residual plot of final design at sea level ($P_0 = 101,325$ Pa).

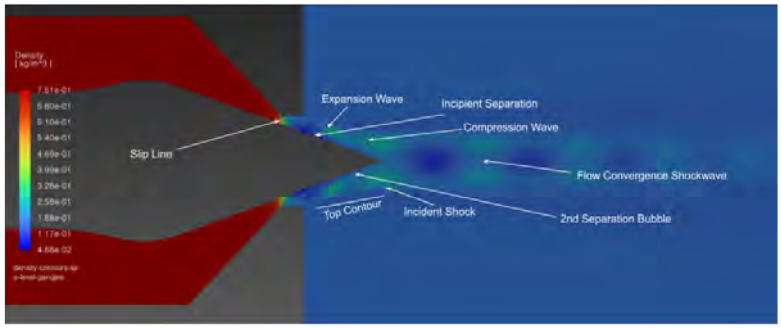

Figure 10: Labeled density contours of exhaust flow at sea level ($P_0 = 101,325$ Pa).

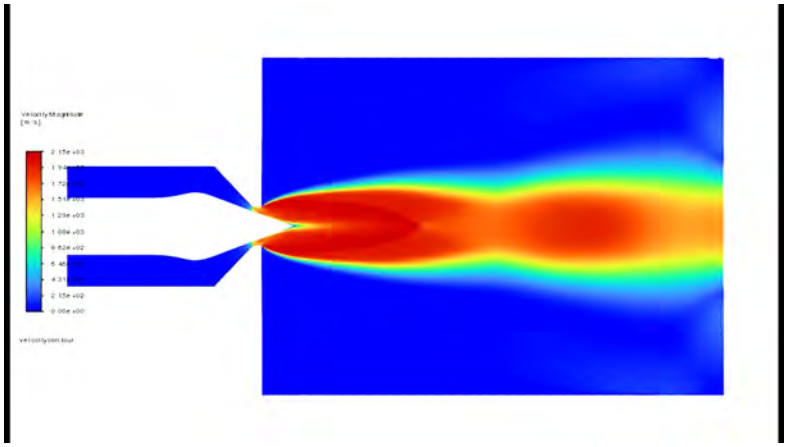

Figure 11: Velocity contours of final design at 25 km ($P_0 = 2,511$ Pa).

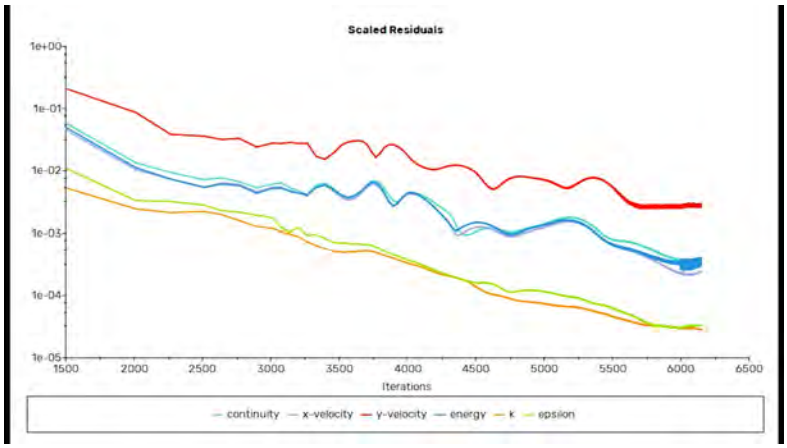

Figure 12: Residual plot of final design at 25 km ($P_0 = 2,511$ Pa).

The limitations of the simulation techniques used are significant and must be acknowledged when interpreting these results. The k–ϵ turbulence model assumes fully developed, isotropic turbulence and relies on time-averaged Reynolds equations, which makes it poorly suited for capturing the transient, highly compressible flow structures that occur in rocket exhausts. In particular, the model cannot accurately resolve shock–boundary-layer interactions or the local separation and reattachment dynamics that often govern thrust efficiency on aerospike surfaces [21]. This limitation causes the shock–boundary interactions to have the "smeared" appearance shown in Figure 10.

The simulations were conducted under a frozen-flow assumption, meaning chemical reactions and dissociation processes were not modeled in the gas dynamics. This simplification neglects variations in local specific heat ratios, gas composition, and temperature-dependent transport properties that occur in real rocket exhausts, especially near the throat and within expansion regions. As a result, the computed flow field represents an idealized equilibrium state rather than the true thermochemical behavior of the propellant gases.

Two-dimensional planar modeling also introduces geometric constraints, preventing accurate prediction of three-dimensional effects such as radial pressure gradients and azimuthal asymmetries in the exhaust annulus. Together, these assumptions limit the quantitative fidelity of the results, though the overall flow structure and qualitative expansion behavior remain meaningful for design evaluation.

To address some of these limitations, I used a DES (Detached Eddy Simulation) turbulence model to refine the shock boundaries observed in the k–ϵ simulations. Once the simulation converged below 1×10^{-4}, I set the solver to transient mode with a time step of 1×10^{-6} seconds and an initial Courant

number of 0.5. The transient convergence criteria were set to oscillations between 1×10^{-4} and 1×10^{-5}, with 30 iterations per time step. To correct a large oscillation, the Courant number was later reduced to 0.15. The scaled residuals are shown in Figure 13. The y^+ of the mesh was 2.04 which indicates that it can properly simulate wall shear and flow separation.

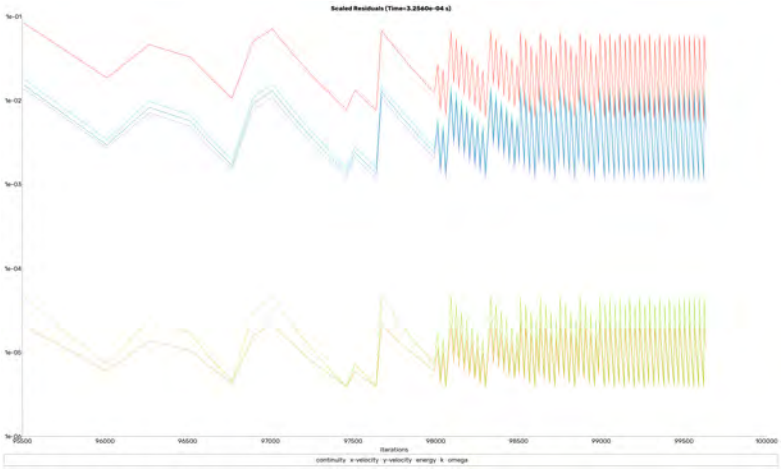

Figure 13: Scaled residuals for detached eddy simulation.

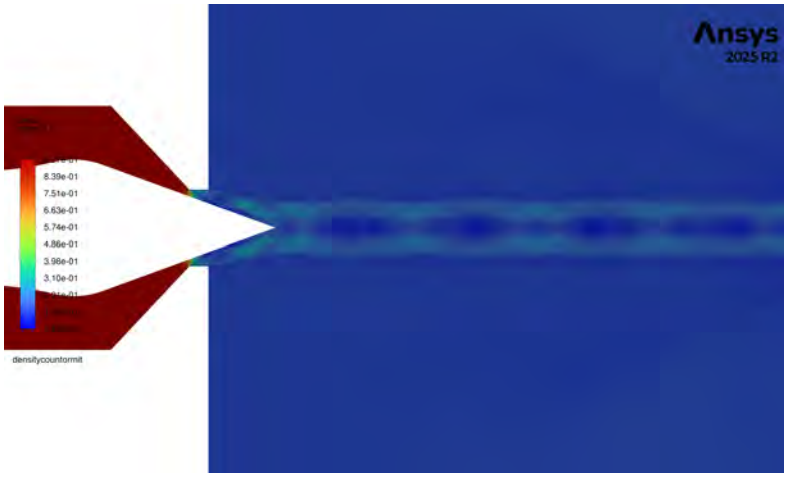

Figure 14: Density contours for detached eddy simulation.

To check whether the exhaust flow reattached or remained separated as it appeared in Figure 14, I used the Turbulent Kinetic Energy (TKE) contours of the simulation, shown in Figure 15, to determine whether the flow reattached

to the spike. The contours indicated that, while a small low-pressure pocket formed at the end of the spike, it did not break up the exhaust flow. This behavior is ideal for a spike operating at sea level, as the exhaust flow can expand and move the bubble further down the spike as altitude increases. For this reason, I selected this configuration as the final engine contour. Additionally, because of the manufacturing tolerances of the available printer, any further refinement of the contour would likely have a negligible impact on performance compared to defects in the printed surface, such as layer lines and small geometric deformations created during the printing process.

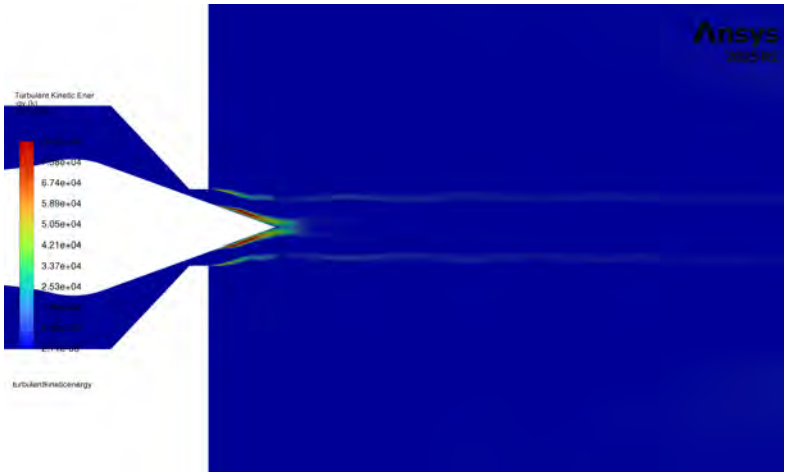

Figure 15: Turbulent kinetic energy contours for detached eddy simulation.

4.6 Wall Pressure Distribution and Separation Analysis

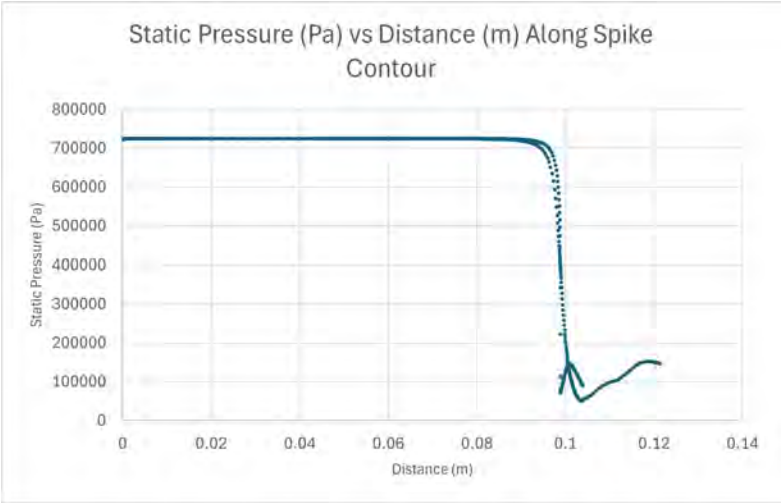

Figure 16: Static pressure along spike vs x-coordinate.

The wall-pressure distribution along the aerospike in Figure 16 shows a nearly constant plateau of approximately 7×10^5 Pa from the throat through the mid-spike region ($x < 0.09$), indicating that the flow remains fully attached and expands nearly isentropically. A sharp pressure drop occurs near $x = 0.09$, marking the onset of separation as the local static pressure falls toward ambient conditions. Downstream of this point, small oscillations in the pressure trace correspond to the recirculation bubble and weak recompression shocks observed in the transient contours. The separated region stabilizes near $P_{\text{base}} \approx 1 \times 10^5$ Pa, yielding a base-to-chamber pressure ratio of approximately $P_{\text{base}}/P_{\text{chamber}} \approx 0.14$. This ratio is consistent with expected behavior for aerospikes operating at sea-level conditions. The identified separation onset aligns with the turbulent kinetic energy pocket observed in Figure 15.

4.7 Thrust Scaling and Validation

Quantity	Symbol	Value	Units
Pressure force (2-D)	F_{p}	1700.19	N/m
Viscous force (2-D)	F_{v}	2.05	N/m
Total force (2-D)	F_{CFD}	1702.25	N/m
Mean radius	r_{mean}	11.0	mm
Circumference	$C = 2\pi r_{\mathrm{mean}}$	0.0691	m
Scaled thrust	$F_{\mathrm{phys}} = F_{\mathrm{CFD}} C$	**117.8**	**N**

The integrated wall forces obtained from Fluent yielded a pressure thrust of $F_{\mathrm{p}} = 1700.19$ N/m and a viscous drag of $F_{\mathrm{v}} = 2.05$ N/m, giving a total of $F_{\mathrm{CFD}} = 1702.25$ N/m in the two-dimensional axisymmetric domain. Because this result corresponds to thrust per meter of annular circumference, it was scaled by the engine's mean radius of $r_{\mathrm{mean}} = 11$ mm to obtain the equivalent three-dimensional thrust:

$$C = 2\pi r_{\mathrm{mean}} = 2\pi(0.011) = 0.0691 \text{ m}$$

$$F_{\mathrm{phys}} = F_{\mathrm{CFD}} C = 1702.25(0.0691) \approx 117.8 \text{ N}$$

This value agrees within one percent of the 118 N design target predicted by the rocket design equations used in step 3 of the design workflow, confirming that the simulated pressure field accurately reproduces the intended expansion performance of the aerospike nozzle.

4.8 Grid Independence Study

Quantity	Value
Coarse mesh elements	35,755
Coarse mesh min orthogonal quality	0.6437
Coarse mesh max aspect ratio	8.700
Moderate mesh elements	154,921
Moderate mesh min orthogonal quality	0.602
Moderate mesh max aspect ratio	17.04
Turbulence model	Realizable k–ϵ
Residual convergence	$< 1 \times 10^{-4}$
Thrust (DES reference)	117.8 N
Thrust deviation (moderate mesh)	0.17%
Thrust deviation (coarse mesh)	0.058 %

Table 4: Grid independence results showing minimal variation in thrust across meshes. Reports and mesh statistics are detailed in Appendix D (154,921-element) and Appendix E (35,755-element). The small deviations from the DES reference confirm grid independence.

A coarser mesh containing 154,921 elements was generated by proportionally reducing the divisions across all regions of the flow domain (simulation report and mesh statistics provided in Appendix D). A realizable k–ϵ turbulence model was applied to this mesh and solved until residuals fell below 1×10^{-4}. The resulting thrust was within 0.17% of the transient DES prediction of 117.8 N obtained with the 269,886-element mesh, indicating no measurable dependence on grid density.

A third, more reduced mesh containing 35,755 elements (report and statistics in Appendix E) produced a thrust only 0.058% different from the DES result, further confirming consistency across resolutions. The minimal variation among all three meshes demonstrates that the solution is grid independent. The fine mesh accurately captures the thrust and pressure distributions necessary for further design analysis. With the spike contour verified in simulation, I then proceeded to designing the engine and cooling channels.

5 Design

This section outlines the design process of the aerospike rocket engine and test stand. It does not cover the test stand electronics or data acquisition system, as those were handled by my partner.

5.1 Regenerative Cooling System Overview

The engine was designed in Fusion 360 and incorporates a square-walled single spiral channel in both the spike and the case, as shown in Figure 19. Through these channels, liquid propane was circulated before injection into the combustion chamber through radial injection ports. I chose not to use oxygen as a coolant in the regenerative cooling system because the phase change of propane from liquid to gas within the cooling channels utilizes its latent heat of vaporization, improving the overall effectiveness of the cooling system.
Using data collected by Oval-Trujillo et al., I assumed a thermal conductivity of 0.366 W/m·K for the resin used in the engine [22]. The resulting modeling of boundary-layer formation, conducted using Rocket Propulsion Analysis software near the engine walls, yielded an average heat flux vector in a boundary-layer equilibrium state of 343.14 kW/m^2, as shown in Figure 17. I assumed that the heat flux experienced by the aerospike was equivalent to that of the combustion chamber and contracting section of a bell nozzle, since the surface area of the spike outside the engine cowling is proportionally small compared to the total surface area. As the heat flux decreases with the pressure drop along the exhaust flow, the external spike region contributes minimally to total engine heating.

Although literature regarding the specific heat capacity (c_p) of high-temperature SLA liquid resins is limited, I conducted calorimetry testing on samples of cured resin and referenced known performance data from non-thermally robust analogous materials produced by the same manufacturer. From these tests, I determined an estimated modeling value of 2300 J/kg·K for c_p.

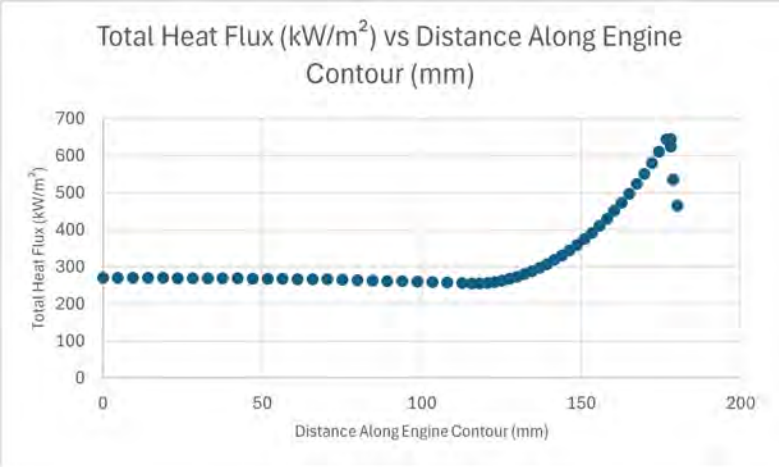

Figure 17: Total heat flux plot along spike contour.

The steady-state and transient thermal behavior of the regeneratively cooled engine were estimated using the average convective heat flux from the combus-

tion gases, the coolant flow rate, and the material properties of the engine body. The governing relations are summarized below:

$$\dot{Q}_{\text{in}} = \bar{q}'' A, \qquad \Delta T_{\text{cool}} = \frac{\dot{Q}_{\text{in}}}{\dot{m}_{\text{cool}} c_{p,\text{cool}}}, \qquad \Delta T_{\text{wall}} = \frac{\bar{q}'' t_w}{k_w}$$

$$\frac{dT}{dt} = \frac{\dot{Q}_{\text{in}}}{m c_p},$$

Parameter	Symbol	Value	Units / Description
Average heat flux	$\bar{q}''$	3.43×10^5	W/m^2
Exposed wall area	A	0.0366	m^2
Wall thickness	t_w	0.0012	m
Wall thermal conductivity	k_w	0.314	W/m·K (polymer)
Engine mass	m	0.406	kg
Material density	ρ	1200	kg/m^3
Specific heat of wall	c_p	2300	J/kg·K
Coolant mass flow rate	$\dot{m}_{\text{cool}}$	0.04519	kg/s
Coolant specific heat	$c_{p,\text{cool}}$	2500	J/kg·K (liquid propane)
Chamber pressure	P_c	0.732	MPa (105 psi)
Effective film coefficient	h	20,000	$\text{W/m}^2\text{·K}$

Table 5: Input parameters used in the thermal analysis of the regeneratively cooled aerospike engine.

Thermal Analysis Calculations

The total heat absorbed by the engine wall from the combustion gases is obtained from the average heat flux and exposed surface area:

$$\dot{Q}_{\text{in}} = \bar{q}'' A \tag{1}$$

$$\dot{Q}_{\text{in}} = (3.43 \times 10^5\,\text{W/m}^2)(0.0366\,\text{m}^2) = 1.25 \times 10^4\,\text{W} = 12.5\ \text{kW}$$

The temperature rise of the coolant as it passes through the channels is:

$$\Delta T_{\text{cool}} = \frac{\dot{Q}_{\text{in}}}{\dot{m}_{\text{cool}} c_{p,\text{cool}}} \tag{2}$$

$$\Delta T_{\text{cool}} = \frac{1.25 \times 10^4}{(0.0452)(2500)} = 110\ \text{K}$$

The conductive temperature drop across the wall thickness can be estimated using one-dimensional steady-state conduction:

$$\Delta T_{\text{wall}} = \frac{q'' t_w}{k_w} \tag{3}$$

$$\Delta T_{\text{wall}} = \frac{(3.43 \times 10^5)(0.00120)}{0.314} = 1.31 \times 10^3 \text{ K} = 1310 \text{ K}$$

To estimate the transient heating rate of the wall if no cooling is present:

$$\frac{dT}{dt}_{\text{no cool}} = \frac{\dot{Q}_{\text{in}}}{m c_p} \tag{4}$$

$$\frac{dT}{dt}_{\text{no cool}} = \frac{1.25 \times 10^4}{(0.406)(2300)} = 13.4 \text{ K/s}$$

Including regenerative cooling, the effective net heating rate of the structure is reduced according to the energy removed by the coolant:

$$\frac{dT}{dt}_{\text{cooled}} = \frac{\dot{Q}_{\text{in}} - \dot{m}_{\text{cool}} c_{p,\text{cool}} \Delta T_{\text{cool}}}{m c_p} \tag{5}$$

Because nearly all of the wall heat is absorbed by the coolant, the residual term is small:

$$\frac{dT}{dt}_{\text{cooled}} = 1.03 \text{ K/s}$$

These relations yield the results summarized in Table 6.

Quantity	**Result**	**Meaning**
$\dot{Q}_{\text{in}}$	12.5 kW	Total heat transferred from combustion gases to wall
ΔT_{cool}	111 K	Temperature rise of liquid propane coolant
ΔT_{wall}	1310 K	Gas-to-coolant wall temperature gradient
$\frac{dT}{dt}$ (no cooling)	13.4 K/s	Bulk warm-up rate without active cooling
$\frac{dT}{dt}$ (cooled)	1.03 K/s	Effective warm-up rate under regenerative cooling

Table 6: Summary of calculated thermal parameters for the regeneratively cooled engine.

With regenerative cooling active, approximately 13.4 kW of heat is absorbed from the exhaust flow, producing a coolant temperature rise of about 111 K. The engine wall experiences a transient heating rate of roughly 1.03 K/s as the coolant approaches full flow, compared to 13.4 K/s in an uncooled condition.

Although this was higher than I aimed for, I recognized that the low mass flow rate of C_3H_8 due to the small engine, as well as the relatively low thermal

passivity of the resin used, diminished the efficacy of the regenerative cooling system. As the transient heating of the engine is horizontally asymptotic above the heat deflection temperature of the resin, the model indicates that the engine can only be used for short-duration testing.

5.2 Engine CAD

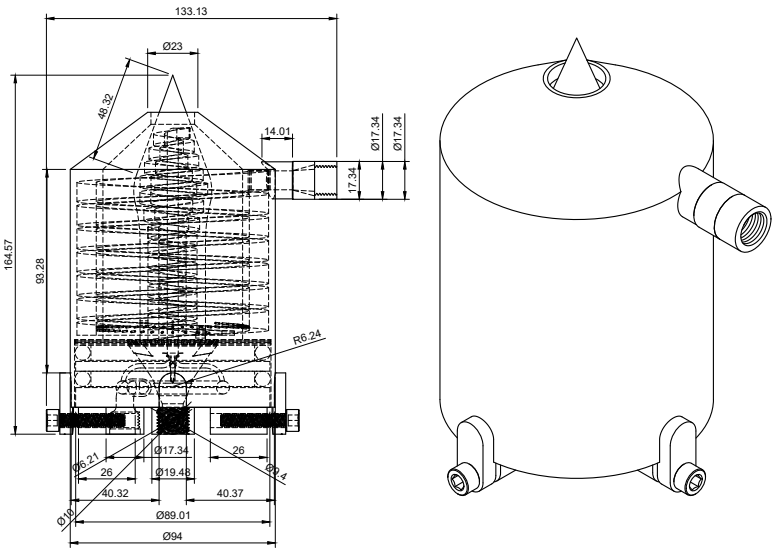

Figure 18: Engine sketch.

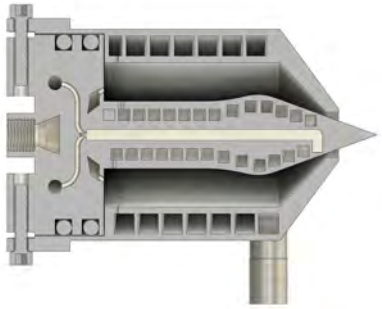

Figure 19: Engine CAD cut through.

5.3 Engine Embodiment

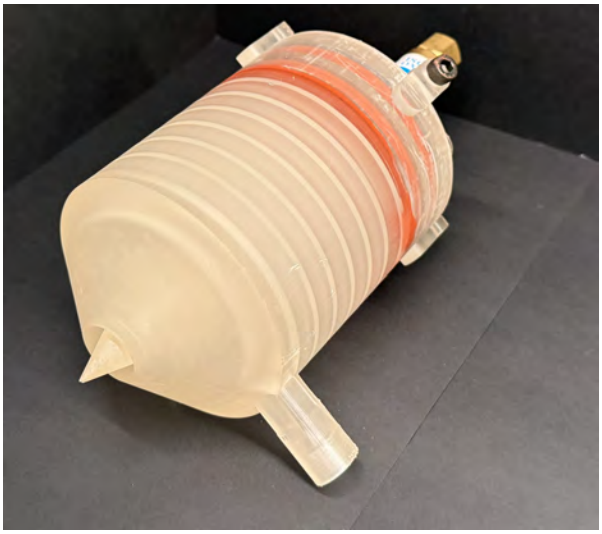

Figure 20: Printed engine.

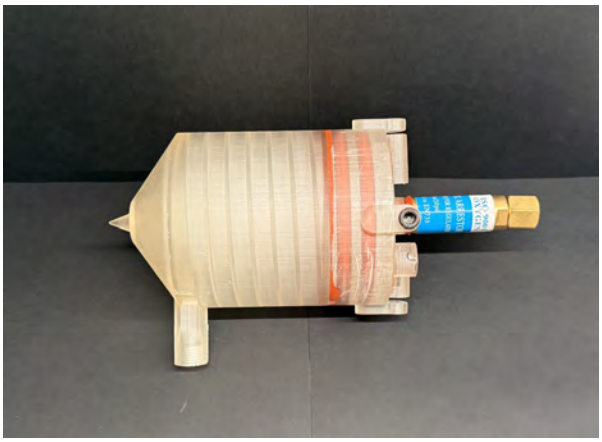

Figure 21: Printed engine.

6 Test Stand

The testing system was designed to ensure the safety of all participants and surrounding observers while collecting accurate data on the performance and effectiveness of the rocket engine. The test system architecture consisted of three primary components: the test stand on which the engine was mounted, the fuel and oxidizer tanks and delivery lines, and the electronics system (not discussed).

6.1 Test Stand Design

The first version of the test stand was constructed from fire-resistant Medium Density Fibreboard (MDF). This material was selected for its low cost and ease of fabrication. As shown in Figure 22, Version 1 of the stand consisted of perpendicularly attached MDF panels, the aerospike engine mounted on a ball-bearing drawer rail, and the fuel and oxidizer delivery system connected to the engine. The ball-bearing rail allowed for thrust measurements by enabling the engine to move linearly against a strain gauge, with a small metal plate attached to the engine positioned to contact the sensor. The MDF was coated with aluminum tape to improve fire resistance.

Figure 22: Version 1 test stand render.

I generated the test stand architecture using CAD modeling to visualize and optimize the system layout prior to fabrication. To mitigate the risk of backflow caused by high-pressure combustion gas expansion, redundant flashback arrestors were installed in both the oxidizer and fuel lines as seen in Figure 23. Additionally, check valves were integrated into the propane fuel feed to ensure unidirectional flow and mechanical isolation of upstream components. These components were selected for their reliability and rated flow performance under high-temperature and high-pressure transient conditions.

To predict the mass flow rate to the engine under expected steady-state operating conditions, I applied Bernoulli's equation with empirical pressure-drop modeling across the check valves. Assuming incompressible, steady flow and negligible elevation change, I used Eqn. 6 to determine the regulator pressures needed to deliver nominal mass flow rates to the engine for a design chamber pressure of 723kPa.

$$\dot{m} = C_f A \sqrt{2\rho \left(P_{\text{in}} - P_{\text{out}}\right)} \tag{6}$$

- $\dot{m}$ is the predicted mass flow rate (kg/s),
- $C_f = 1.2$ is the valve discharge coefficient,
- A is the internal flow area of the valve (m^2),
- ρ is the fluid density (kg/m^3),

- P_{in} and P_{out} are the upstream and downstream static pressures across the valve (Pa).

These calculations informed valve selection, regulator setpoints, and flow safety margins, ultimately supporting a predictive model of engine fuel supply under dynamic test conditions. Remote servo-controlled two-way valves were also implemented to regulate propellant delivery and maintain operator safety by allowing full system actuation from a shielded distance.

I adhered to strict safety procedures to ensure that the propellant delivery system could reliably withstand the loads associated with testing as well as potential failure modes. The oxidizer feed systems were constructed using brass and stainless steel, as both materials are non-reactive with the propellants at the expected pressures and temperatures during operation. All components were cleaned in an ultrasonic cleaner using isopropyl alcohol as the cleaning agent. After cleaning, parts were stored in a controlled environment and treated in accordance with CGA G-4.1 cleaning procedures [23]. All pipe connections were sealed with PTFE tape, which is compatible with both oxygen and propane [24]. Flashback arrestors were installed as needed to prevent back-propagating flame conditions, as shown in Figure 23.

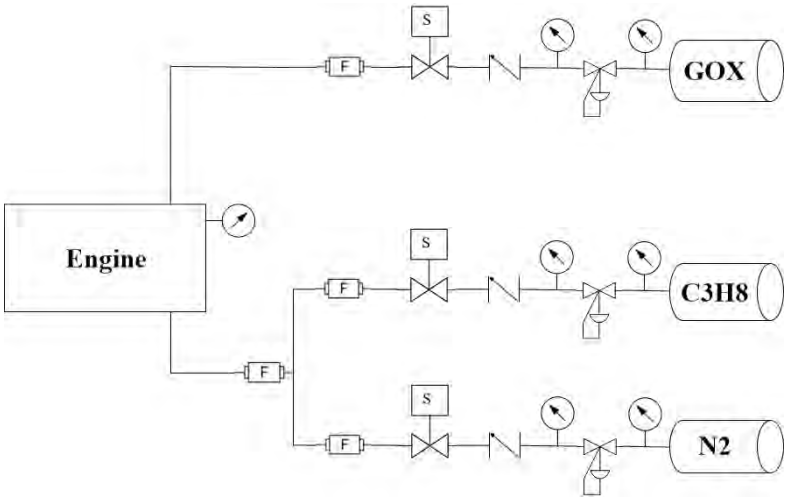

Figure 23: Plumbing diagram of test stand.

For the third test, I designed and built a new test stand constructed from aluminum extrusion profiles, rendered in Figure 24, to replace the original MDF frame, substantially improving both fire resistance and mechanical stability. The linear slide used previously was replaced with a solid mount between the engine and a higher-capacity force sensor, which produced higher-quality data. The flammability of the electronics system was also reduced to improve reusability and lower costs by wrapping all sensors and circuit boards with aluminum

tape initially, followed by application of a silicone conformal coating. The sixth test encountered a hard-start event, an uncontrolled ignition characterized by rapid over-pressurization and structural failure, a phenomenon documented in both amateur and professional aerospace propulsion testing [25].

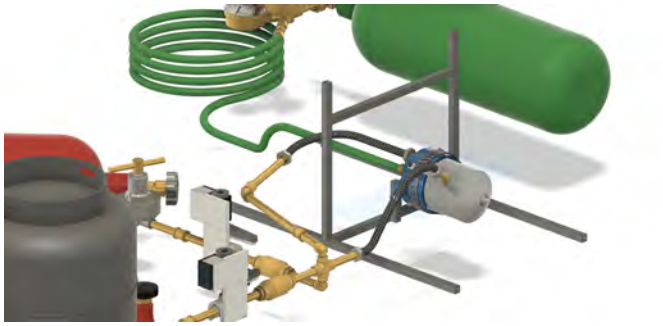

Figure 24: Render of Version 2 test stand.

7 Test Procedure

The testing procedures used to gather data closely followed those described in *How to Design, Build, and Test Small Liquid-Fuel Rocket Engines* [16].

All engine tests were conducted under controlled outdoor conditions in accordance with strict safety and operational protocols. The following procedure was executed for each test to ensure reliable performance, personnel safety, and data integrity.

Prior to ignition, the test team confirmed that the firing zone was fully cleared of all personnel, obstructions, and non-essential equipment. All operators and observers were positioned either at a remote operator station equipped with large chemical fire extinguishers or at a minimum distance of 50 feet from the test stand. No personnel were permitted to remain in direct line of sight with the combustion chamber during ignition or burn phases.

Following area clearance, the ignition system was verified from the remote station by sending a low-voltage test pulse to confirm ignitor continuity and circuit readiness. The ignition element, a cotton ball soaked in hydrocarbon fuel, was inserted into the combustion chamber through the nozzle using a rigid armature and secured in place. The entire ignitor insertion process was completed before the re-energization of any high-voltage systems.

All electronic control and sensor systems were powered on and verified for operational integrity. A calibrated spring scale was then attached to the engine and used to apply a known force of 1 kg to the strain gauge on the

test stand. This force was used to calibrate the raw strain-gauge data. Functional checks were performed on valve actuation and pressure regulator feedback through the remote microcontroller interface. A full pressure and leak test was conducted on both the purge line and the propane fuel line by pressurizing each to twice the nominal operating pressure using inert gas. Any detected leaks or pressure instability resulted in immediate test stand lockout and procedural restart.

For high-pressure oxygen handling, the supply tank was uncoiled and positioned at a standoff distance greater than 15 m from the test stand to mitigate explosion risk. The nitrogen purge system was then armed remotely by opening the isolation valve and confirming line pressure through an in-line pressure gauge.

Once the mechanical and control systems were validated, the ignitor was remotely activated from the operator panel. Immediately following visible ignition, oxygen flow was initiated at a low rate and gradually increased. Propane was then introduced via a slowly opened solenoid valve to allow controlled chamber pressurization. If ignition failed, indicated by the absence of a visible flame plume, all flows were terminated immediately, and the cause of the misfire was diagnosed before resuming operations.

Upon successful sustained combustion, oxygen and propane flow rates were rapidly and simultaneously increased to their peak target levels. Fine-tuning of the oxidizer-to-fuel ratio was performed in real time by monitoring flame characteristics such as plume length, color, and acoustic tone. Adjustments were made to achieve optimal combustion efficiency and plume symmetry.

After the engine operated for the designated runtime, feed pressures were smoothly reduced to zero in a controlled ramp-down sequence. The engine was then purged with high-purity nitrogen for at least five minutes to remove residual fuel and oxidizer vapors from the chamber and lines.

Following the purge, the high-pressure oxygen supply was safely disconnected and isolated, followed sequentially by the propane and nitrogen canisters. Post-test operations included collection of sensor and video data, along with physical inspection of the test hardware. All equipment was disassembled, and any debris resulting from the test was cleared from the area. The site was restored to a neutral and safe condition before the conclusion of operations.

8 Results

I conducted a total of six trials across three versions of the engine to validate performance. The thrust curves from the best trial of each version are shown in the graphs below. I estimate that all thrust measurement errors for Versions 2 and 3 are within ±2%, which is more than double the manufacturer's specified accuracy and accounts for data deviations caused by load-cell exposure to elevated temperatures during rocket tests, even after shielding methods were implemented to reduce heat transfer to the sensors. For Version 1, the data accuracy is estimated at ±10%, as a less precise strain gauge was used. During testing, all engine versions produced convergent exhaust plumes with contours closely matching the CFD simulation results, as shown in Figs. 25, 26, and 27.

Figure 25: Version 1 engine exhaust plume at maximum mass flow rate.

Figure 26: Version 2 engine exhaust plume at maximum mass flow rate.

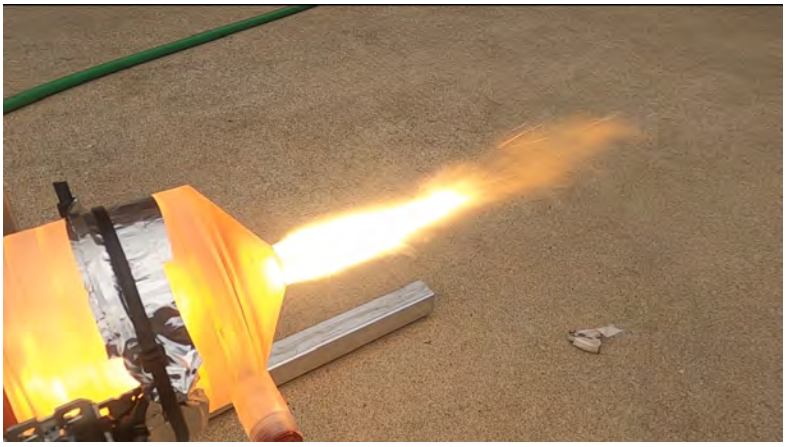

Figure 27: Version 3 engine exhaust plume at maximum mass flow rate.

8.1 Thrust

Engine Version	**Peak Thrust (N)**	**Total Impulse (N·s)**	I_{sp} **(s)**
V1	87.91 ± 8.7	609.13 ± 60.90	144.54 ± 2.89
V2	107.37 ± 2.14	883.12 ± 17.60	163.96 ± 3.27
V3	113.27 ± 2.26	303.69 ± 3.03	181.46 ± 3.63

Table 7: Thrust and efficiency summary for all engine versions.

The thrust data collected across all tests were promising. The first engine design, with thrust data shown in Figure 28, produced 87.91 N peak thrust with a total impulse of 609.13 N·s. The second engine, with thrust data in Figure 29, produced 107.36 N peak thrust and a total impulse of 883.12 N·s during the fourth consecutive test, all conducted within ten minutes. No graphs were produced for Version 2 tests 1–3 because those runs were used to tune fuel feed and regulator pressure values. I did not record thrust data during those runs because prolonged exposure to the exhaust plume would have negatively affected strain-gauge accuracy. Those early runs were not intended to produce significant thrust, so their omission does not change the main experimental conclusions. The third engine, with thrust data in Figure 30, produced 113.27 N peak thrust at a total impulse of 303.69 N·s.

Engine performance varied for several reasons. Version 1 experienced a structural failure of the spike supports as mass flow rate increased, which ended the test prematurely.

Version 2 tests used a new strain gauge with an 11× higher sampling rate than the initial design. Version 2 also included reinforced spike-wall connecting struts that were actively cooled and routed fuel into the spike through a separate cooling-channel matrix before injection into the combustion chamber via radial injectors. I tested Version 2 four times in succession to tune startup procedures and mixture ratios. The fourth test is shown in Figure 29 and displays a flat line during the nominal burn. This apparent steady output was caused by a data acquisition saturation in the strain gauge system, whose maximum reading was below the engine output. Consequently I only have a lower bound for that run, but I expect the true peak thrust to be similar to the peak measured in Version 3. Version 2 operated fuel-rich throughout the tests, which reduced specific efficiency relative to Version 3. The Version 2 test series ended early due to a structural failure of the engine cowling caused by the metal slide heating from proximity to the exhaust plume, which cracked an uncooled section of the throat (see Figure 33).

Version 3 used optimized oxidizer injectors that replaced a single injector ring with two angled rings converging 0.5 cm from the injector plate, producing a four-stream converging behavior and improved combustion efficiency. Also, a different strain gauge was utilized with a higher fidelity, sample rate, and larger measurement range. During the Version 3 test I observed a mid-test hard-start event. The test reached peak flow rates, but a small fissure in the engine wall allowed a rapid influx of liquid propane into the combustion chamber, which overextended the flame plume beyond the nozzle. I terminated propellant flow immediately. The accumulated excess propellant then caused an undesired detonation in the chamber and complete structural failure of the engine. I shut off feed, purged the engine with high-pressure nitrogen, and the flames were extinguished within one second. I maintained a low-pressure purge flow for ten minutes post-event to allow residual liquid propane to vaporize and

any lingering oxygen to disperse.

I used the failure to collect empirical data on debris-field formation and fragment sizes to refine safety zones and shielding. From post-test inspection and site measurements I estimated a maximum debris-field radius of 10 m. The forward enclosure successfully contained fragments and prevented shrapnel from impacting the test-stand electronics or areas behind the stand.

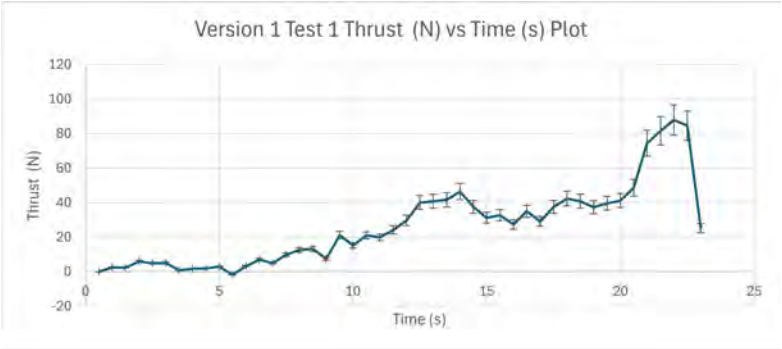

Figure 28: Thrust data plot for version 1 test 1.

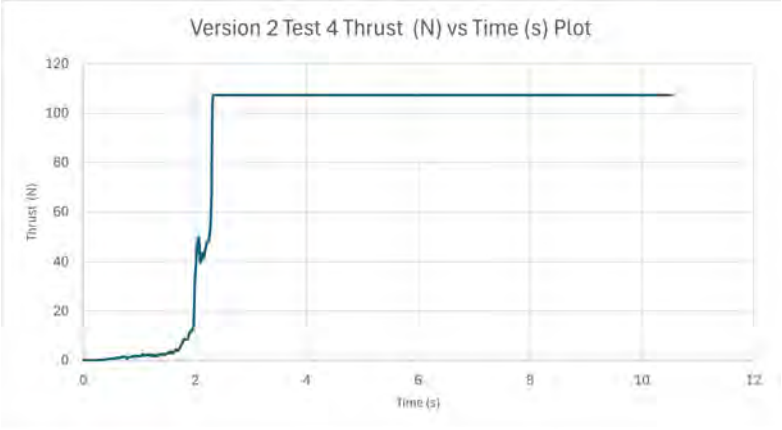

Figure 29: Thrust data plot for version 2 test 4.

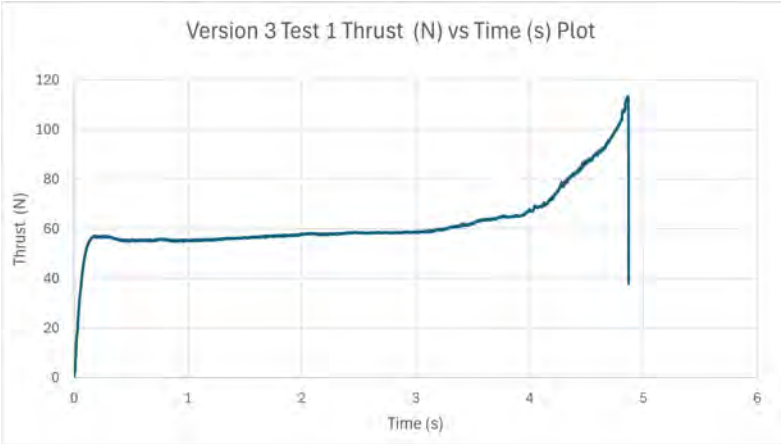

Figure 30: Thrust data plot for version 3 test 1.

8.2 Efficiency

The final engine achieved a specific impulse of 181.46 s, corresponding to an efficiency of approximately 93.46%. However, this value may be skewed because it derives ΔP values from a gauge rather than a calibrated pressure transducer. This results in an accuracy of $\pm 2\%$ at the pressures measured, according to the manufacturer's specifications. If the ΔP between the regulator and the engine was significantly greater than predicted, the total mass flow rate delivered to the engine would have been higher than expected, leading to a lower calculated I_{sp}.

8.3 Thermal Performance

The thermal data obtained from engine testing were highly promising. I measured a 55% decrease in engine wall temperature between the regeneratively cooled and solid-wall designs. The engine's external wall temperature increased at a rate of $2.405 \pm 0.024\, K/s$, which is close to the expected value but indicates that the regenerative cooling channel was slightly less effective than predicted. Additionally, the uncooled section of the engine increased in temperature at 9.39 $\pm$ 0.093 K/s, which is 30% lower than the expected value of 13.4 K/s. These results indicate that the chamber pressure likely did not reach its target value, as a higher chamber pressure would increase engine heating speed by minimizing the size of the near-wall boundary layer. Also, it is possible that the resin has a lower thermal conductivity than expected, so resisted both cooling via the regenerative cooling channels, and heating via exposure to combustion gasses. Nonetheless, the efficacy of the regenerative cooling system is evident and allowed for the repeat firing of Version 2 before structural failure.

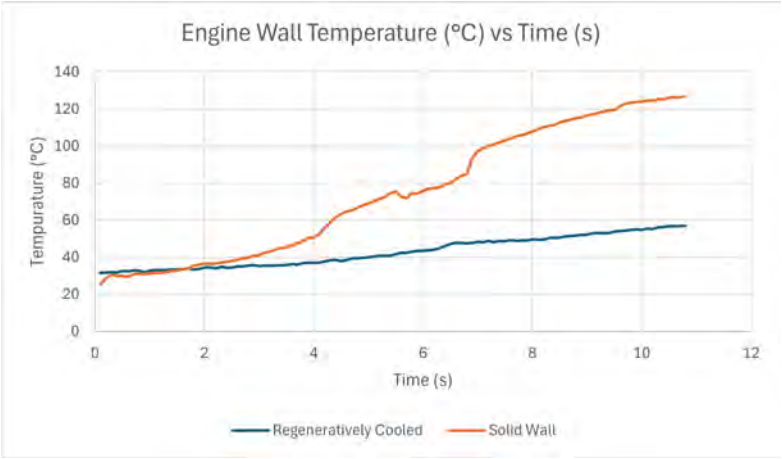

Figure 31: Temperature vs time plot of regeneratively cooled and solid wall sections of aerospike rocket engine of equivalent thickness.

8.4 Failure Modes and Improvements

Each test allowed me to iteratively improve the engine design through a continuous build–break–improve cycle. In the first test, the supports of the central spike were too thin, resulting in structural failure during the Version 1 test, as shown in Figure 32. To correct this, I thickened the supports and increased the proportion of total coolant flow directed through the spike relative to the case. In Version 2, the engine cowling that contacted the metal slide cracked due to radiative heating from the slide, as shown in Figure 33. To address this issue, I fully redesigned the test stand for the Version 3 tests.

Figure 32: Version 1 spike failure.

Figure 33: Version 2 engine crack.

9 Conclusion

The engine I developed for this project successfully completed four consecutive static-fire tests. Each test consumed $10.87 in propellant and purge gases. The measured performance and the iterative design improvements demonstrate a viable rapid prototyping workflow for small bipropellant aerospike engines within the scope of this study.

The per-unit fabrication cost for the printed prototype totaled $87.99. The primary cost items are listed in Table 8.

Item	Cost (prices subject to vary due to tariffs) ($)
Bolts (hardware)	1.48 [26]
Resin (High Temp V2)	72.67 [27]
Flashback arrestor	7.50 [28]
Two O-rings	5.99 [29]
High-Temperature gasket maker	0.35 [30]
Total	**87.99**

Table 8: Per-unit fabrication cost breakdown for the printed prototype.

The production time for a complete engine, including 3D printing, UV curing, post-processing, dimensional verification, and basic stress checks, was approximately 30 hours. This project successfully demonstrated the production speed benefits, cost benefits, and validity of a regeneratively cooled polymer rocket engine. Further testing and a larger data set could strengthen these findings further as only 3 tests resulted in significant data collection.

References

[1] Neufeld, M. J., *The Rocket and the Reich: Peenemünde and the Coming of the Ballistic Missile Era*, Free Press, New York, NY, 1995.

[2] Sutton, G. P. and Biblarz, O., *Rocket Propulsion Elements*, John Wiley & Sons, Hoboken, NJ, 9th ed., 2017.

[3] Monokrousos, N., Könözsy, L., Pachidis, V., Sozio, E., and Rossi, F., "Numerical Solution of LOx Flow in a Liquid Rocket Engine Additively Manufactured Cooling Channel," *Proceedings of the 34th Congress of the International Council of the Aeronautical Sciences (ICAS 2024)*, ICAS / Curran Associates, Florence, Italy, 2024, pp. 4726–4741.

[4] Cárdenas, I. R., Lain, S., and López, O. D., "A Review of Aerospike Nozzles: Current Trends in Aerospace Applications," *Aerospace*, Vol. 12, No. 6, 2025.

[5] Huzel, D. K. and Huang, D. H., *Modern Engineering for Design of Liquid-Propellant Rocket Engines*, Vol. 147 of *Progress in Astronautics and Aeronautics*, American Institute of Aeronautics and Astronautics, Washington, DC, 1992.

[6] Metal AM (Metal Additive Manufacturing) Magazine, "Making the unmakeable: How 3D printing is bringing the aerospike rocket engine to life," https://www.metal-am.com/articles/making-the-unmakeablehow-3d-printing-is-bringing-the-aerospike-rocket-engine-to-life/, 2022, Accessed: 2025-10-27.

[7] AM, M. and coverage, P. A., "Pangea Aerospace and partners develop 3D-printed aerospike demonstrators," 2022, Also see Pangea Aerospace press coverage and ESA multimedia (2025). Accessed: 2025-10-27.

[8] European Space Agency (ESA), "Firing up Arcos — the European aerospike engine," 2025.

[9] LEAP 71, "LEAP 71 and Aconity3D unveil 3D-printed aerospike rocket engine at Formnext 2024," https://leap71.com/2024/11/21/leap-71-and-aconity3d-unveil-3d-printed-aerospike-rocket-engine-at-formnext-2024/, 2024, Accessed: 2025-10-27.

[10] TCT / VoxelMatters / LEAP 71 press coverage, "LEAP 71 hot-fires 3D-printed aerospike rocket engine," https://www.tctmagazine.com/additive-manufacturing-3d-printing-news/leap71-successfully-hot-fire-tests-aerospike-engine/, 2025, TCT and VoxelMatters coverage of LEAP 71 hot-fire activity. Accessed: 2025-10-27.

[11] Song, J. and Sun, B., "Thermal-structural analysis of regeneratively-cooled thrust chamber wall in reusable LOX/Methane rocket engines," *Chinese*

Journal of Aeronautics, Vol. 30, No. 4, 2017, pp. 805–817, Accessed: 2025-10-27.

[12] Formlabs Inc., "High Temp Resin: Technical Data Sheet (V2, FLHTAM02)," https://formlabs-media.formlabs.com/datasheets/1801087-TDS-ENUS-0P.pdf, 2018, Prepared 2020-10-07; Rev. 02 dated 2018-12-05. Accessed: 2025-10-26.

[13] Formlabs Inc., *Form 3 User Manual*, Formlabs Inc., 2021, Rev. 02 (July 2021). Accessed: 2025-10-26.

[14] Nair, P. P., Suryan, A., and Kim, H. D., "Computational study on flow through truncated conical plug nozzle with base bleed," *Propulsion and Power Research*, Vol. 8, No. 2, 2019, pp. 108–120.

[15] Formlabs Inc., *High Temp Resin: Material Data Sheet*, Formlabs Inc., September 2016, Rev. 02, December 05 2018.

[16] Krzycki, L. J., *How to Design, Build, and Test Small Liquid-Fuel Rocket Engines*, Rocketlab Publishing, Berea, OH, 1967.

[17] "Rocket Test Cell (Cryogenic) - The University of Alabama in Huntsville," 2017.

[18] Ramirez, I., Lain, S., and Lopez Mejia, O., "A Review of Aerospike Nozzles: Current Trends in Aerospace Applications," *Aerospace*, Vol. 12, 06 2025, pp. 519.

[19] Aukerman, C. A., "Plug Nozzles - The Ultimate Customer Driven Propulsion System," Tech. Rep. 187169, NASA Lewis Research Center / Sverdrup Technology, Inc., 1991, Accessed: 2025-10-27.

[20] VDEngineering, "VDEngineering YouTube Channel," https://www.youtube.com/@VDEngineering, 2025, Accessed: 2025-10-25.

[21] Bernard, P. S., "Limitations of the near-wall k-epsilon turbulence model," *AIAA Journal*, Vol. 24, 1986, pp. 619–622.

[22] Oval Trujillo, A., Rodríguez, A., Pérez-Artieda, M., Dung, Y., and Alegria, P., "Experimental measurement of thermal conductivity of stereolithography photopolymer resins," *SN Applied Sciences*, Vol. 4, No. 8, 08 2022.

[23] "Cleaning of Equipment for Oxygen Service (CGA G-4.1)," 2018, Seventh edition.

[24] Clean-Fit Products, The Mill-Rose Company, "Blue Monster "OXY-Clutch" Green Oxygen Tape: Compatible with gaseous or liquid oxygen and many other gases and liquids," 2025, Accessed: 2025-10-26.

[25] Mills, T. R. and Breen, B. P., "Computer Modeling of Rocket Engine Ignition Transients: Final Report," Tech. Rep. NASA CR-140361, National Aeronautics and Space Administration, Jet Propulsion Laboratory, Pasadena, CA, 1970.

[26] "MYWISH M6 × 25 mm Black Oxide Stainless Steel Socket Head Cap Screws (20-Pack)," Home Depot product listing, 2025.

[27] Formlabs Inc., "High Temp Resin – Product Page," https://formlabs.com/store/materials/high-temp-resin/, 2025.

[28] "Acetylene/Propane Flashback Arrestor Set Regulator End – Oxygen and Acetylene Compatible (Amazon product ID B0BPS9H72H)," https://www.amazon.com/Uenede-Acetylene-Flashback-Arrestors-Regulator/dp/B0BPS9H72H, 2025.

[29] "High-Temperature High-Purity Silicone O-Rings, Item 9396K922," https://www.mcmaster.com/high-temperature-o-rings/, 2025, Specific item no. 9396K922; Accessed: 2025-10-26.

[30] "Permatex 81630 Ultra Red High Temperature Gasket Maker (3 oz)," https://www.amazon.com/Permatex-81630-Ultra-Temperature-Gasket/dp/B08CRY2BJB, 2025, Accessed: 2025-10-25; price about US$7.18 at time of access.

A Appendix A: Practice Solution 1 CEA Printout

```
            THEORETICAL ROCKET PERFORMANCE ASSUMING EQUILIBRIUM

          COMPOSITION DURING EXPANSION FROM INFINITE AREA COMBUSTOR

Pin =  2050.0 PSIA
CASE = Practice_1_____

            REACTANT                    WT FRACTION      ENERGY      TEMP
                                         (SEE NOTE)     KJ/KG-MOL      K
FUEL        CH4                          1.0000000         0.000      0.000
OXIDANT     O2(L)                        1.0000000    -12979.000     90.170

O/F=    2.20000  %FUEL= 31.250000  R,EQ.RATIO= 1.813302  PHI,EQ.RATIO= 1.813302

                CHAMBER   THROAT     EXIT
Pinf/P            1.0000   1.7663   139.00
P, BAR            141.34   80.020   1.0168
T, K             3358.75  3090.27  1395.66
RHO, KG/CU M    8.5280 0 5.2794 0 1.4995-1
H, KJ/KG         -278.86 -1181.09 -5793.05
U, KJ/KG        -1936.25 -2696.80 -6471.19
G, KJ/KG        -46604.4 -43803.7 -25042.7
S, KJ/(KG)(K)    13.7925  13.7925  13.7925

M, (1/n)          16.850   16.952   17.112
(dLV/dLP)t      -1.00794 -1.00478 -1.00000
(dLV/dLT)p        1.1414   1.0918   1.0001
Cp, KJ/(KG)(K)    3.9594   3.5472   2.4727
GAMMAs            1.1826   1.1906   1.2446
SON VEL,M/SEC     1400.0   1343.3    918.7
MACH NUMBER        0.000    1.000    3.615

PERFORMANCE PARAMETERS

Ae/At                       1.0000   14.242
CSTAR, M/SEC                1993.0   1993.0
CF                          0.6740   1.6663
Ivac, M/SEC                 2471.6   3525.1
Isp, M/SEC                  1343.3   3320.9


MASS FRACTIONS

*CO              0.47718  0.47356  0.39058
*CO2             0.10737  0.11314  0.24360
COOH             0.00002  0.00001  0.00000
*H               0.00116  0.00076  0.00000
HCO              0.00007  0.00003  0.00000
*H2              0.03563  0.03597  0.04234
HCHO,formaldehy  0.00001  0.00001  0.00000
HCOOH            0.00001  0.00001  0.00000
H2O              0.36754  0.37061  0.32348
*O               0.00035  0.00012  0.00000
*OH              0.01033  0.00565  0.00000
*O2              0.00031  0.00011  0.00000

 * THERMODYNAMIC PROPERTIES FITTED TO 20000.K

NOTE. WEIGHT FRACTION OF FUEL IN TOTAL FUELS AND OF OXIDANT IN TOTAL OXIDANTS
```

B Appendix B: Practice Solution 2 CEA Printout

```
            THEORETICAL ROCKET PERFORMANCE ASSUMING EQUILIBRIUM

          COMPOSITION DURING EXPANSION FROM INFINITE AREA COMBUSTOR

Pin =    42.0 PSIA
CASE = Version_1_____

            REACTANT                    WT FRACTION      ENERGY      TEMP
                                         (SEE NOTE)     KJ/KG-MOL      K
FUEL        CH4                          1.0000000         0.000     0.000
OXIDANT     O2(L)                        1.0000000    -12979.000    90.170

O/F=    2.20000  %FUEL= 31.250000  R,EQ.RATIO= 1.813302  PHI,EQ.RATIO= 1.813302

                CHAMBER   THROAT     EXIT
Pinf/P            1.0000   1.7398   2.8500
P, BAR            2.8958   1.6644   1.0161
T, K             3041.25  2869.50  2715.41
RHO, KG/CU M    1.8748-1 1.1560-1 7.5281-2
H, KJ/KG         -278.86 -1104.97 -1793.22
U, KJ/KG        -1823.41 -2544.74 -3142.92
G, KJ/KG        -48138.4 -46261.7 -44525.0
S, KJ/(KG)(K)    15.7368  15.7368  15.7368

M, (1/n)          16.371   16.571   16.728
(dLV/dLP)t      -1.02321 -1.01668 -1.01167
(dLV/dLT)p        1.4539   1.3436   1.2520
Cp, KJ/(KG)(K)    7.2184   6.2352   5.3637
GAMMAs            1.1435   1.1476   1.1542
SON VEL,M/SEC     1329.0   1285.4   1248.1
MACH NUMBER        0.000    1.000    1.394

PERFORMANCE PARAMETERS

Ae/At                      1.0000   1.1342
CSTAR, M/SEC               1948.8   1948.8
CF                         0.6596   0.8930
Ivac, M/SEC                2405.5   2515.9
Isp, M/SEC                 1285.4   1740.3


MASS FRACTIONS

*CO             0.47492  0.47097  0.46741
*CO2            0.11108  0.11729  0.12289
*H              0.00345  0.00264  0.00196
HCO             0.00001  0.00000  0.00000
*H2             0.03484  0.03520  0.03563
H2O             0.34693  0.35508  0.36026
*O              0.00251  0.00131  0.00064
*OH             0.02405  0.01633  0.01062
*O2             0.00221  0.00118  0.00058

 * THERMODYNAMIC PROPERTIES FITTED TO 20000.K

NOTE. WEIGHT FRACTION OF FUEL IN TOTAL FUELS AND OF OXIDANT IN TOTAL OXIDANTS
```

C Appendix C: Version 1 CEA Printout

```
            THEORETICAL ROCKET PERFORMANCE ASSUMING EQUILIBRIUM

          COMPOSITION DURING EXPANSION FROM INFINITE AREA COMBUSTOR

Pin =   105.0 PSIA
CASE = Actual_Version1

            REACTANT                    WT FRACTION      ENERGY      TEMP
                                         (SEE NOTE)     KJ/KG-MOL      K
FUEL        C3H8                         0.5000000   -108944.593    235.000
FUEL        C3H8(L)                      0.5000000   -128228.000    231.076
OXIDANT     O2                           1.0000000      -678.913    275.000

O/F=    2.00000  %FUEL= 33.333333  R,EQ.RATIO= 1.814171  PHI,EQ.RATIO= 1.814171

                CHAMBER   THROAT     EXIT
Pinf/P            1.0000   1.7557   7.1400
P, BAR            7.2395   4.1234   1.0139
T, K             3027.58  2817.46  2277.91
RHO, KG/CU M    5.3045-1 3.2758-1 1.0090-1
H, KJ/KG         -910.58 -1648.75 -3235.09
U, KJ/KG        -2275.35 -2907.50 -4239.98
G, KJ/KG        -42686.1 -40525.0 -34666.5
S, KJ/(KG)(K)    13.7984  13.7984  13.7984

M, (1/n)          18.445   18.610   18.847
(dLV/dLP)t      -1.01256 -1.00784 -1.00135
(dLV/dLT)p        1.2465   1.1637   1.0336
Cp, KJ/(KG)(K)    4.5766   3.8972   2.6695
GAMMAs            1.1634   1.1729   1.2124
SON VEL,M/SEC     1260.1   1215.1   1103.8
MACH NUMBER        0.000    1.000    1.953

PERFORMANCE PARAMETERS

Ae/At                       1.0000   1.8296
CSTAR, M/SEC                1818.8   1818.8
CF                          0.6680   1.1855
Ivac, M/SEC                 2251.0   2622.2
Isp, M/SEC                  1215.1   2156.2


MASS FRACTIONS

*CO             0.55301  0.54864  0.53456
*CO2            0.12914  0.13602  0.15814
*H              0.00176  0.00119  0.00024
HCO             0.00001  0.00000  0.00000
*H2             0.02774  0.02820  0.02972
H2O             0.27474  0.27849  0.27658
*O              0.00081  0.00031  0.00001
*OH             0.01208  0.00687  0.00074
*O2             0.00071  0.00028  0.00001

 * THERMODYNAMIC PROPERTIES FITTED TO 20000.K

NOTE. WEIGHT FRACTION OF FUEL IN TOTAL FUELS AND OF OXIDANT IN TOTAL OXIDANTS
```

Appendix D: Moderate Mesh Simulation Report

The following pages contain a section of the ANSYS Fluent simulation validation report for the moderate-density mesh used in the regeneratively cooled aerospike nozzle study. This section of the report includes detailed mesh quality metrics (orthogonal quality and aspect ratio), residual convergence histories, mass flow rate, and thrust values, the latter of which is used to confirm grid independence.

Geometry and Mesh

Mesh Size

Cells	Faces	Nodes
154921	310892	155972

Mesh Quality

Name	Type	Min Orthogonal Quality	Max Aspect Ratio
solid-surface_body	Quad Cell	0.60233618	17.038705

Orthogonal Quality

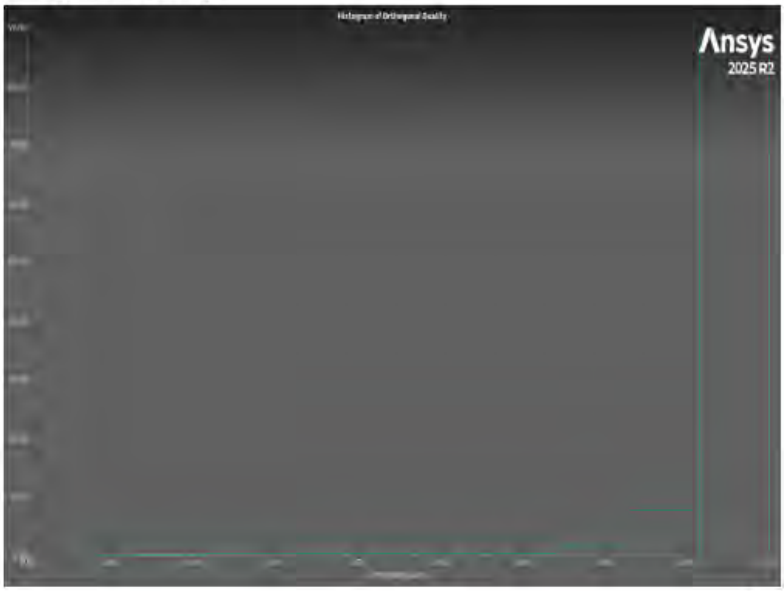

Report Definitions

Mass Flow Rate	0.05159346	kg/s
Thrust Output	1705.236	N
cfl-number	5	

Plots

Residuals

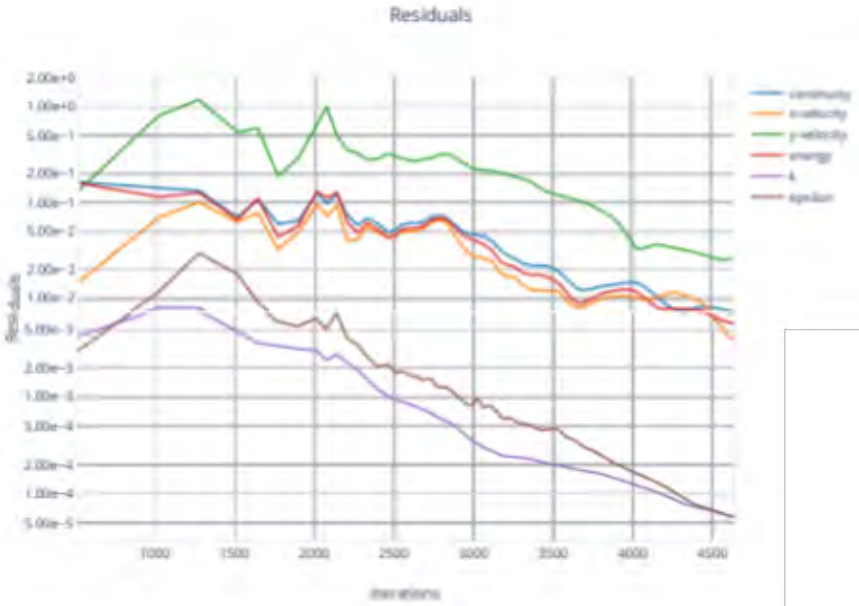

Appendix E: Coarse Mesh Simulation Report

The following pages contain a section of the ANSYS Fluent simulation validation report for the coarse mesh used in the regeneratively cooled aerospike nozzle study. This section of the report includes detailed mesh quality metrics (orthogonal quality and aspect ratio), residual convergence histories, mass flow rate, and thrust values, the latter of which is used to confirm grid independence.

Geometry and Mesh

Mesh Size

Cells	Faces	Nodes
36755	74098	37344

Mesh Quality

Name	Type	Min Orthogonal Quality	Max Aspect Ratio
solid-surface_body	Quad Cell	0.64374498	8.7009122

Orthogonal Quality

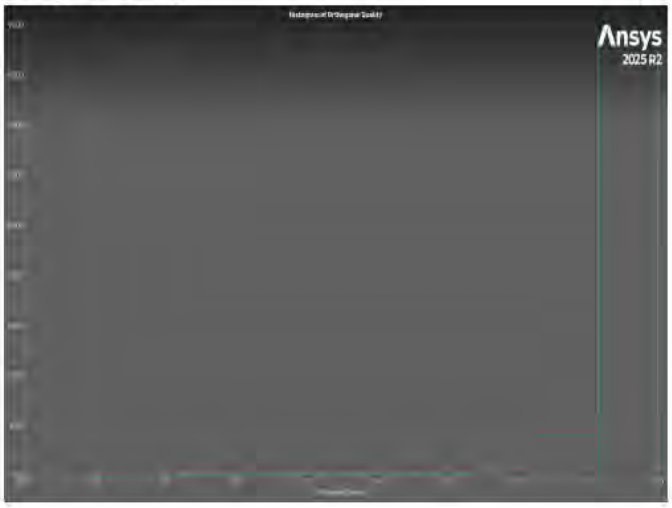

Report Definitions

Mass Flow Rate	0.05225108	kg/s
Thrust Output	1701.662	N
cfl-number	5	

Plots

Residuals